Rigorous interference and diffraction analysis of diffractive optic elements using the Finite-Difference Time-Domain method

J. Francés[a], C. Neipp[a,b], M. Pérez-Molina[a,b], A. Beléndez[a,b]

[a] *University of Alicante*
Department of Physics, Systems Engineering and Signal Theory
San Vicente del Raspeig Ap. 99, E-03080
Alicante, (Spain)
[b] *University of Alicante*
University Institute of Physics Applied to Sciences and Technologies
San Vicente del Raspeig Ap. 99, E-03080
Alicante, (Spain)

Abstract

The Finite-Difference Time-Domain (FDTD) method has proven to be a useful tool to analyze electromagnetic scattering phenomena. In this work, the FDTD method is applied at optical wavelengths. More precisely, we present the results obtained using the FDTD algorithm to simulate the performance of optical devices such as volume diffraction gratings. The Perfectly Matched Layers (PML), Total-Field Scattered-Field formulation (TF/SF) and Near-Field to Far-Field transformation (NF/FF) are some add-ons included in order to correctly calculate the far field distribution obtained from the numerical near-field values computed in the simulation region. These values in the near-field region are computed by illuminating the grating with of a plane wave at the Bragg angle of incidence. In addition, we compare the results obtained by the FDTD method to those obtained using the Rigorous Coupled Wave Theory (RCWT) applied to diffraction gratings. As will be seen in this paper there is good agreement between the two approaches, thus validating our FDTD implementation.

Keywords: Finite-Difference Time-Domain, Holography, diffraction grating, Rigorous Coupled Wave Theory, diffraction efficiency, angular efficiency
PACS: 42.25.-p, 42.25.Fx, 42.25.Hz, 42.40.Eq, 42.40.Lx

1. Introduction

In recent decades diffractive optical elements have been used in many applications such as the manufacture of lenses and mirrors [1, 2], broadband communications [3], optical computation [4] or information storage [5]. Because of the small sizes of these optical elements, rigorous electromagnetic computational methods are needed to obtain their diffraction efficiency. There are several numerical methods applied to solve electromagnetic problems such as the finite-element method [6], the boundary-element method [7, 8, 9] and the boundary-integral method [10] which require solving of a large system of equations. The Finite-Difference Time-Domain method (FDTD) [11, 12] is based on a time-marching algorithm that has proven accurate in predicting microwave scattering from complicated objects, for instance. The FDTD method solves the differential Maxwell equations, substituting the time and spatial derivatives with central-difference approximation providing the transient electromagnetic field and wide band frequency analysis via a single simulation.

In this paper the FDTD method is applied to rigorously analyze holographic volume gratings for the near-field distribution. Furthermore, far-field distributions can be obtained from the FDTD-calculated near-field distributions using of the rigorous near to far-field transformations in two and three dimensions [13, 14, 15]. It is well known that diffraction gratings with feature sizes comparable to the wavelength of light must be treated electromagnetically because the scalar diffraction theories, including Fourier and Fresnel approximations, no longer apply [16]. Although some work has been done on the FDTD method for periodic structures [17, 18, 19] and thin-film gratings [20], in this paper a specific application of the FDTD method is developed to study the diffraction and transmission efficiencies of volume holographic gratings.

In Section 2 the elemental theory related to the FDTD method is introduced. In this section special considerations predicting the performance of gratings and other optical devices, including boundary conditions and far field transformation are described. For simplicity TM polarization was considered in all of the experiments (electric field parallel to the z-axis, and magnetic field in the xy plane). In many applications an infinitely large one-dimensional structure in the z direction can be assumed, and this is illuminated by a TM plane wave. In such a case, the solutions of Maxwell's curl equations can be reduced to a two-dimensional problem. All gratings simulated in Section 4 are studied in two dimensions.

Email address: jfmonllor@ua.es (J. Francés)

All the values obtained via the FDTD algorithm are compared with those obtained by means of a standard method based on the RCW theory, which has proven to be accurate when applied to diffraction gratings [21]. This method predicts the efficiency of the different orders that propagate inside a grating. For decades researchers in the field of Holography have used the analytical expressions deduced by Kogelnik [22] to estimate the theoretical predictions of phase and amplitude, transmission and reflection volume holograms. This theory assumes that only two orders propagate inside the hologram. In this paper we make use of our implementation of the RCW method to study the influence of the various Fourier component of the electrical permittivity on the efficiency of the grating. This method is detailed in section 3.

2. Basic numerical formulation

Light propagation is described by Maxwell's time-dependent curl equations in *Gaussian units*[13, 23]:

$$\frac{\partial \widetilde{\mathbf{D}}}{\partial t} = \frac{1}{\sqrt{\epsilon_0 \mu_0}} \left(\nabla \times \mathbf{H} - \sigma \widetilde{\mathbf{E}} \right), \quad (1)$$

$$\widetilde{\mathbf{D}}(\omega) = \epsilon_r^*(\omega) \cdot \widetilde{\mathbf{E}}, \quad (2)$$

$$\frac{\partial \mathbf{H}}{\partial t} = -\frac{1}{\sqrt{\epsilon_0 \mu_0}} \nabla \times \widetilde{\mathbf{E}} - \frac{\sigma_m}{\mu_0} \mathbf{H}, \quad (3)$$

where ϵ_0 is the electrical permittivity in farads per meter, ϵ_r^* is the medium's relative complex permittivity constant, μ_0 is the magnetic permeability in henrys per meter, σ_m is an equivalent magnetic resistivity in ohms per meter and σ is the electric conductivity in siemens per meter. The flux density is denoted by $\mathbf{D}$ and both $\mathbf{D}$ and $\mathbf{E}$ are normalized with respect to the vacuum impedance η_0, using

$$\widetilde{\mathbf{E}} = \sqrt{\frac{\epsilon_0}{\mu_0}} \mathbf{E}, \quad (4)$$

$$\widetilde{\mathbf{D}} = \sqrt{\frac{1}{\epsilon_0 \mu_0}} \mathbf{D}. \quad (5)$$

The FDTD algorithm used here is based on the Yee[24] lattice as depicted in Fig. 1.a). The electric field components $\mathbf{E}$ and the magnetic field components $\mathbf{H}$ are centered in a three-dimensional cell so that every $\mathbf{E}$ component is surrounded by four circulating $\mathbf{H}$ components, and every $\mathbf{H}$ component is surrounded by four circulating $\mathbf{E}$ components [14, 25].

To solve Maxwell's curl equations in two dimensions for TM polarization, Eqs.(1-3) are discretized by using central-difference expressions for both the time and the space derivatives. For two dimensions, the Yee cell is still useful and only an *xy* plane containing $\mathbf{H}$ fields is necessary, as can be seen in Figure 1.b). Eqs.(1-3) are reduced to the following taking into account a nonmagnetic and lossless medium:

$$\widetilde{D_z}\big|_{i,j}^{n+1/2} = \widetilde{D_z}\big|_{i,j}^{n-1/2} + \frac{\Delta t}{\Delta y \sqrt{\mu_0 \epsilon_0}} \left(H_y\big|_{i+1/2,j}^{n} - H_y\big|_{i-1/,j}^{n} \right) - \frac{\Delta t}{\Delta x \sqrt{\mu_0 \epsilon_0}} \left(H_x\big|_{i,j+1/2}^{n} + H_x\big|_{i,j-1/2}^{n} \right), \quad (6)$$

$$H_x\big|_{i,j+1/2}^{n+1} = H_x\big|_{i,j+1/2}^{n-1} - \frac{\Delta t}{\Delta z \sqrt{\mu_0 \epsilon_0}} \left(E_z\big|_{i,j+1}^{n+1/2} - E_z\big|_{i,j}^{n+1/2} \right), \quad (7)$$

$$H_y\big|_{i+1/2,j}^{n+1} = H_y\big|_{i+1/2,j}^{n-1} + \frac{\Delta t}{\Delta z \sqrt{\mu_0 \epsilon_0}} \left(E_z\big|_{i+1,j}^{n+1/2} - E_z\big|_{i,j}^{n+1/2} \right). \quad (8)$$

Here, Δx and Δy are, respectively, the lattice space increments in the x and y coordinate directions, and i and j are integers that denote the position of sample points in the x and y directions, respectively. The time increment is represented by Δt and is related to the integer n to localize a determined observation interval. At the material boundaries the continuity conditions for the electric and magnetic fields are satisfied implicitly within the accuracy of the numerical discretization. In the time domain a leapfrog algorithm is applied [14]. The electric and magnetic fields are calculated alternately at intervals of $\frac{1}{2}\Delta t$. The time step has an upper bound to ensure the numerical stability of the algorithm [14, 13, 26]. This is summarized by the well-known "Courant condition":

$$\Delta t \leq \frac{\Delta}{\sqrt{p} c_0}, \quad (9)$$

where p is the dimension of the simulation and $\Delta = \Delta x = \Delta y$. Throughout this paper we will for simplicity determine Δt as

$$\Delta t \leq \frac{\Delta}{2 \cdot c_0}. \quad (10)$$

2.1. Perfectly matched layer absorption condition

In order to simulate unbounded free space, absorbing boundary conditions are included in the region in which the optical device is totally enclosed. Usually, when calculating the $\mathbf{E}$ field, we need to know the surrounding $\mathbf{H}$ values. At the edge of the grid the values at one side are unknown, arbitrary and assumed to be null. As a consequence, reflected waves would go inward in order to keep the boundary conditions mentioned previously. This phenomenon causes an unpredictable field pattern in the simulation region. The perfectly matched layer absorbing boundary conditions proposed by Berenger [27], which have been found to be effective and to cause only slight reflection error, are used in our study. To apply the PML to our algorithm, the electric and magnetic fields are split into scalar components so that independent lossy factors can be assigned to each electromagnetic field term. The effect of this is to create a nonphysical absorbing medium adjacent to the outer FDTD mesh boundary that has a wave impedance independent of the angle of incidence and frequency of the outgoing scattered waves. There have been numerous approaches to this problem [14][26][28][29].

In this paper, a slight deviation from the Berenger method will be made by introducing fictitious conductivities associated with $\mathbf{D}$ and $\mathbf{H}$, instead of $\mathbf{E}$ and $\mathbf{H}$. The basic idea of this formalism is to create a medium that is lossy and minimize the amount of reflection between free air and the PML region. The reflection is determined by the intrinsic impedance of the two media. Considering a wave propagating in a medium A which impinges upon medium B, the amount of reflection is determined by:

$$\Gamma = \frac{\eta_A - \eta_B}{\eta_A + \eta_B}. \quad (11)$$

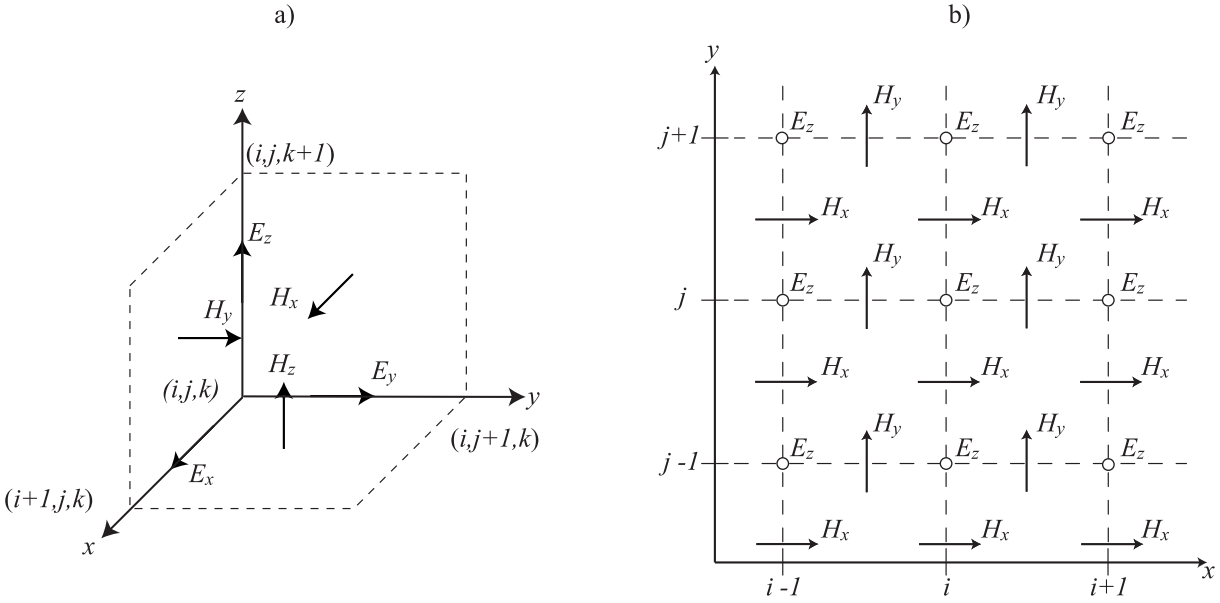

Figure 1: a) Unit cell in 3-D FDTD method. b) Spatial grid in 2-D FDTD method.

where η_A and η_B are the intrinsic impedances of the two media which are determined by the dielectric constants ϵ and permeabilities μ of the two media

$$\eta = \sqrt{\frac{\mu}{\epsilon}} \tag{12}$$

Making both ϵ and μ complex, the medium becomes lossy. In order to obtain this effect, fictitious dielectric constants and permeabilities $\epsilon^*_{F_z}$,$\mu^*_{F_x}$ and $\mu^*_{F_y}$ are added to Eqs.(1-3). These fictitious values used to implement the PML are different from the real values of $\epsilon^*_r(\omega)$ which are specified by the medium. Taking into account that in the PML region, nonreal lossy and magnetic material will be placed, Eqs.(1-3) can be rewritten adding fictitious PML layers:

$$jwD_z\epsilon^*_{F_z}(x)\epsilon^*_{F_z}(y) = c_0\left(\frac{\partial H_y}{\partial x} - \frac{\partial H_x}{\partial y}\right), \tag{13}$$

$$D_z(w) = \epsilon^*_r(w)\cdot E_z(w), \tag{14}$$

$$jwH_x\mu^*_{F_x}(x)\mu^*_{F_x}(y) = -c_0\left(\frac{\partial E_z}{\partial y}\right), \tag{15}$$

$$jwH_y\mu^*_{F_y}(x)\mu^*_{F_y}(y) = c_0\left(\frac{\partial E_z}{\partial x}\right). \tag{16}$$

For the correct behavior of the PML, two conditions must be fulfilled [30]:

1. The impedance going from the background medium to the PML must be constant,

$$\eta_0 = \eta_m = \sqrt{\frac{\mu^*_{F_x}}{\epsilon^*_{F_x}}} = 1. \tag{17}$$

2. In the direction perpendicular to the boundary (the x direction, for instance), the relative dielectric constant and relative permeability must be the inverse of those in the other directions; i.e.,

$$\epsilon^*_{F_x} = \frac{1}{\epsilon^*_{F_y}} = 1, \tag{18}$$

$$\mu^*_{F_x} = \frac{1}{\mu^*_{F_y}} = 1. \tag{19}$$

We will assume that each of these is a complex quantity of the form [13],[29],[30] and [31]:

$$\epsilon^*_{F_m} = \epsilon_{F_m} + \frac{\sigma_{D_m}}{jw\epsilon_0} = 1 + \frac{\sigma_D}{j\omega\epsilon_0} \quad \text{with} m = x, y, \tag{20}$$

$$\mu^*_{F_m} = \mu_{F_m} + \frac{\sigma_{H_m}}{jw\mu_0} = 1 + \frac{\sigma_D}{j\omega\epsilon_0} \quad \text{with} m = x, y. \tag{21}$$

Rewriting Eq.(14-16)

$$jwD_z\left(1 + \frac{\sigma_D(x)}{jw\epsilon_0}\right)\left(1 + \frac{\sigma_D(y)}{jw\epsilon_0}\right) = c_0 \times \left(\frac{\partial H_y}{\partial x} - \frac{\partial H_x}{\partial y}\right) \tag{22}$$

$$jwH_x\left(1 + \frac{\sigma_D(x)}{jw\epsilon_0}\right)^{-1}\left(1 + \frac{\sigma_D(y)}{jw\epsilon_0}\right) = -c_0\left(\frac{\partial E_z}{\partial y}\right), \tag{23}$$

$$jwH_y\left(1 + \frac{\sigma_D(x)}{jw\epsilon_0}\right)\left(1 + \frac{\sigma_D(y)}{jw\epsilon_0}\right)^{-1} = c_0\left(\frac{\partial E_z}{\partial x}\right). \tag{24}$$

Moving to the time domain, and taking the finite difference approximations, we get the following:

$$C_h|_{i,j} = H_y|^n_{i+1/2,j} - H_y|^n_{i-1/2,j} -$$

$$H_x|^n_{i,j+1/2} + H_x|^n_{i,j-1/2}, \tag{25}$$

$$D_z|^{n+1/2}_{i,j} = C_x|_i C_y|_j Dz|^{n-1/2}_{i,j} + B_x|_i B_y|_j \frac{1}{2} C_h|_{i,j}, \tag{26}$$

$$C_e|_{i,j} = \left[E_z|^{n+1/2}_{i+1,j} - E_z|^{n+1/2}_{i,j}\right], \tag{27}$$

$$I_{H_y}|^{n+1/2}_{i+1/2,j} = I_{H_y}|^{n+1/2}_{i-1/2,j} + A_y|_j C_e|_{i,j}, \tag{28}$$

$$H_y|^{n+1}_{i+1/2,j} = C_x|_{i+1/2} H_y|^n_{i+1/2,j} - B_x|_{i+1/2} \frac{1}{2}\left[C_e|_{i,j} + I_{H_y}|^{n+1/2}_{i+1/2,j}\right], \tag{29}$$

$$C_e|^*_{i,j} = \left[E_z|^{n+1/2}_{i,j} - E_z|^{n+1/2}_{i,j+1}\right], \tag{30}$$

$$I_{H_x}|^{n+1/2}_{i,j+1/2} = I_{H_x}|^{n+1/2}_{i,j+1/2} + A_x|_i C_e|_{i,j}, \tag{31}$$

$$H_x|^{n+1}_{i,j+1/2} = C_y|_{j+1/2} H_x|^n_{i,j+1/2} - B_y|_{j+1/2} \frac{1}{2}\left[C_e|^*_{i,j} + I_{H_x}|^{n+1/2}_{i,j+1/2}\right]. \tag{32}$$

where we used the fact that $\Delta t/\Delta c_0 = 1/2$ and the new parameters are given by

$$A_m|_n = 0.333\left(\frac{n}{N_{\mathrm{PML}}}\right)^3 \tag{33}$$

$$B_m|_n = \left(\frac{1}{1 + A_m|_n}\right), \tag{34}$$

$$C_m|_n = \left(\frac{1 - A_m|_n}{1 + A_m|_n}\right). \tag{35}$$

where, $m = x$ or y and $n = 1, 2, \ldots, N_{PML}$. N_{PML} is the number of cells forming the PML region. Figure 2 shows the effectiveness of a 10-point PML.

2.2. Total-Field Scattered-Field formulation

The incidence of the TM plane wave, whose incidence is assumed to be from air to medium and whose propagation in the FDTD region is determined using the time-marching algorithm, is introduced along the connecting boundary by using a total field/scattered field algorithm [14, 13, 26], where $(\mathbf{E}, \mathbf{H})_{\mathrm{Total}} = (\mathbf{E}, \mathbf{H})_{\mathrm{inc}} + (\mathbf{E}, \mathbf{H})_{\mathrm{scat}}$. An arbitrary angle of incidence was taken into account. A scheme of the simulation region is shown in Fig. 3 for normal incidence.

Applying the TF/SF formulation, a plane wave should not interact with the PML, minimizing the load in that area and reducing the amount of error.

The total field region encloses the scatterers, whereas the scattered field region, where only the scattered field region components are stored, encloses the total field region. As illustrated in Figure 3, in the two-dimensional field every point in the problem space is either in the total field or not; no point lies on the border. In order to confine the incident field in the total field region, special "connecting conditions" are required at the border between two regions.

As can be seen in Figure 3 there are fields that use points outside the total region to calculate the spatial derivatives when updating their values. Therefore, the equations of the fields that are under these constraints need to be reformulated. In addition,

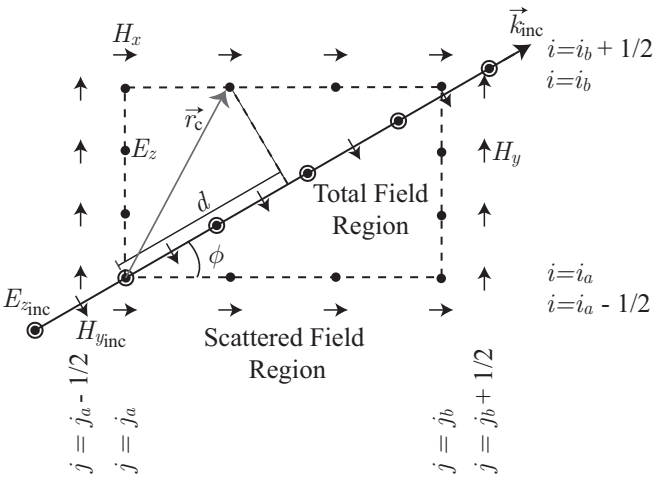

Figure 3: Total field/scattered field scheme for an arbitrary angle of incidence.

this phenomenon is also produced when a field outside the total region uses values from the total region to update its value. The incident array ($E_{z_{\mathrm{inc}}}$ and $H_{y_{\mathrm{inc}}}$) contains all the values needed for this purpose. However, for an arbitrary angle of incidence a linear interpolation can be used, since values of the incident field at the boundaries may not be stored in the memory (this case is shown in Figure 3). This value can be located between two samples of the incident field and calculated from the linear interpolation. If normal incidence is considered, the connecting conditions are defined as follows [14],[29],[32].

1. D_z field component in $j = j_a$ and $j = j_b$.

$$D_z|^{n+1}_{i,j_a} = D_z|^{n+1}_{i,j_a} + \frac{1}{2} H_{x_{\mathrm{inc}}}|_{ja-1/2}, \tag{36}$$

$$D_z|^{n+1}_{i,j_b} = D_z|^{n+1}_{i,j_b} - \frac{1}{2} H_{x_{\mathrm{inc}}}|_{jb+1/2}. \tag{37}$$

2. H_x field component in $j = j_a$ and $j = j_b$.

$$H_x|^{n+1/2}_{i,j_a-1/2} = H_x|^{n+1/2}_{i,j_a-1/2} + \frac{1}{2} E_{z_{\mathrm{inc}}}|_{ja}, \tag{38}$$

$$H_x|^{n+1/2}_{i,j_b+1/2} = H_x|^{n+1/2}_{i,j_b+1/2} - \frac{1}{2} E_{z_{\mathrm{inc}}}|_{jb}. \tag{39}$$

3. H_y field component in $i = i_a$ and $i = i_b$.

$$H_y|^{n+1/2}_{ia-1/2,j} = H_y|^{n+1/2}_{i_a-1/2,j} - \frac{1}{2} E_{z_{\mathrm{inc}}}|_j, \tag{40}$$

$$H_y|^{n+1/2}_{ib+1/2,j} = H_y|^{n+1/2}_{i_b+1/2,j} + \frac{1}{2} E_{z_{\mathrm{inc}}}|_j. \tag{41}$$

After the source is turned on, it is allowed to run for the duration of the simulation, which is long enough for several cycles to scatter off the grating and reach the truncation boundary. In our study a steady-state condition should be reached by making the time steps long enough to ensure that the transient fields have decayed away. Once the steady state is achieved, the field distribution just above the optical device (slit, or holographic grating) can be propagated from the near field (the output plane) to the far field (the observation plane) by using the propagation method for two or three dimensions respectively. For example, the pattern in the far field of a grating, where the

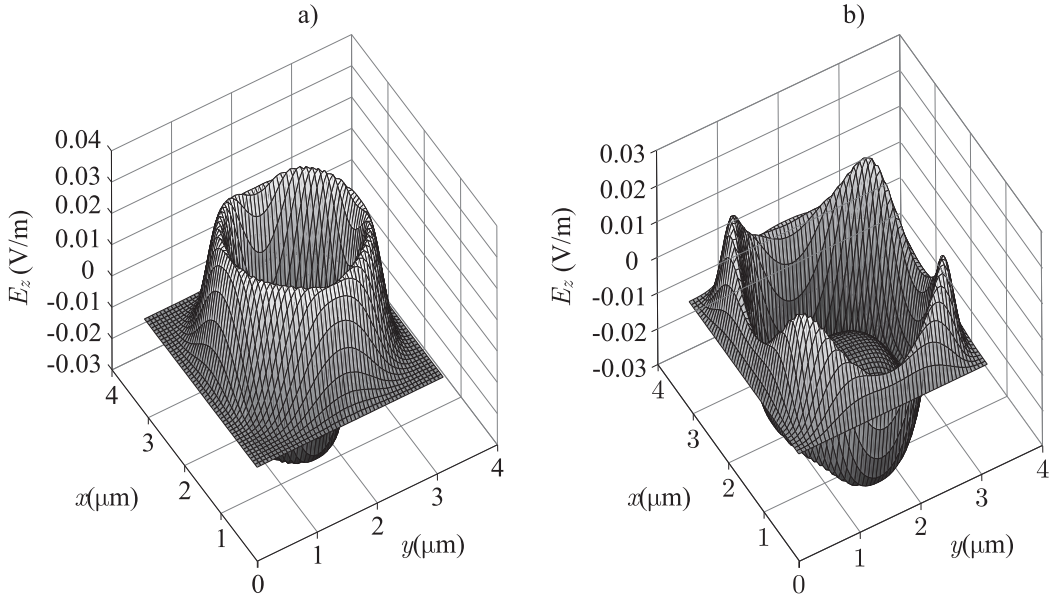

Figure 2: Simulation of a propagating pulse. The effectiveness of the PML is clear. a) $t = 50\Delta t$. b) $t = 80\Delta t$

detector distance P is much larger than Λ/λ, Λ being the grating period, represents the angular distribution of this energy. Simulating the propagation of energy over this distance with the FDTD algorithm, given the discretization requirements of a structure with large dielectric constants and/or detailed structures, requires an extremely large computational grid. However, truncating the mesh closer to the scatterer and calculating the far field response from the values of the field near the scatterer, the performance of the algorithm in terms of memory and time processing is improved.

2.3. Far Field Transformation in two dimensions

In the time domain, the Schelkunoff equivalence principle has been used by many authors in different studies[33, 34, 35, 36, 37] for three-dimensional transient calculations evaluating the Time-Domain Integral Expresion (TDIE) of the fields. Nevertheless, evaluation of the TDIE in two dimensions is not straightforward. Luebbers et al. [38] proposed a mixed frequency/time-domain algorithm which involves two Fourier transformations to obtain the time-domain response. In this paper an approach based on the equivalence principle was implemented to calculate, in the time domain, the transient far-field response of a two-dimensional structure by directly evaluating a two-dimensional form of the TDIE [15]. The procedure leads to an easily implementable algorithm consisting of the numerical evaluation of a two-dimensional integral. This algorithm can be implemented in a marching-on-in-time procedure simultaneously with the FDTD advancing algorithm.

The equivalence principle [23] allows of the actual sources to be substituted by a set of equivalent electric and magnetic surface current densities, located in the near field zone. These currents are given by

$$\mathbf{J}_S(\mathbf{r}', t) = \hat{n} \times \mathbf{H}(\mathbf{r}', t), \tag{42}$$

$$\mathbf{M}_S(\mathbf{r}', t) = -\hat{n} \times \mathbf{E}(\mathbf{r}', t), \tag{43}$$

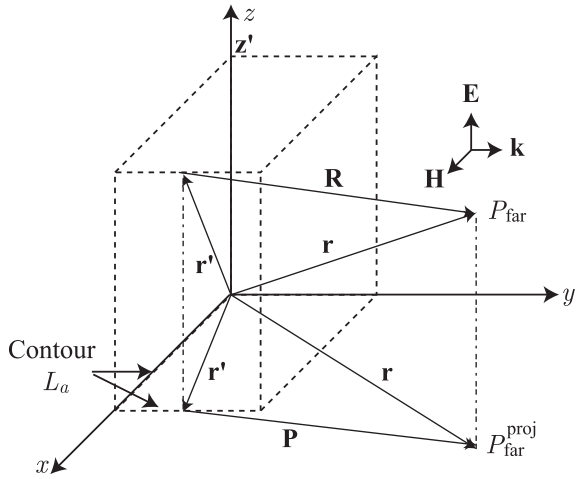

Figure 4: Near to far field transformation scheme.

where $\hat{n}$ is a unit vector normal to the surface and coming out of it and the primed parameters indicate the source while the unprimed parameters are the scattered field. In Fig. 10 the problem is illustrated schematically. It is known how the electric and magnetic current densities contribute to the radiated electric field [39]:

$$\mathbf{E}(\mathbf{r}, t)_{\mathrm{m}}^{\mathrm{rad}} = \frac{\mu_0}{4\pi} \int_{S'} \frac{[\partial_t \mathbf{J}_S(\mathbf{r}', t)]_\tau \times \mathbf{R}) \times \mathbf{R}}{R^3} dS', \tag{44}$$

$$\mathbf{E}(\mathbf{r}, t)_{\mathrm{e}}^{\mathrm{rad}} = -\frac{1}{4\pi c_0} \int_{S'} \frac{[\partial_t \mathbf{M}_S(\mathbf{r}', t)]_\tau \times \mathbf{R}) \times \mathbf{R}}{R^2} dS', \tag{45}$$

where $\mathbf{R} = \mathbf{r} - \mathbf{r}'$ is the vector from the source point to the field point. The total electric field is the sum of the electric and magnetic contributions $\mathbf{E}(\mathbf{r}, t)^{\mathrm{rad}} = \mathbf{E}(\mathbf{r}, t)_{\mathrm{e}}^{\mathrm{rad}} + \mathbf{E}(\mathbf{r}, t)_{\mathrm{m}}^{\mathrm{rad}}$. The fundamental point of the procedure, based on previous studies [40, 15], is to evaluate of the integral along z', taking advantage for the expression of the retarded sources by a time integral us-

ing the translation property of the Dirac delta function. Taking into account this property and manipulating Eqs. (44-45) mathematically we can obtain the final expression for the electric far field:

$$\mathbf{E}(\mathbf{r},t)^{\text{far}} = -\frac{1}{2\pi\sqrt{2}\sqrt{r}}\int_{L_a} dl' \times \int_{t'=-\infty}^{t'=t-R/c_0} \frac{\eta_0 \partial_{t'}\mathbf{J}_S(\mathbf{r}',t) + \partial_{t'}\mathbf{M}_S(\mathbf{r}',t)\times\hat{r}}{\sqrt{c_0(t-t')-R}}dt', \tag{46}$$

where $\hat{r} = \mathbf{r}/r$ and L_a is the conversion contour showed in Fig 10.

Due to the unbounded behavior of the integrand when $t' \to (t - R/c_0)^-$, the time integral is solved by combining numerical and analytical techniques [15, 41].

3. Rigorous Coupled Wave Theory

There are different methods in the literature that precisely describe electromagnetic propagation in volume diffractive elements [42, 43, 44, 45, 46, 47].

In this section, we briefly review the RCW theory for the case of lossless sinusoidal transmission diffraction gratings. For more details see Refs. [21], [48].

In this case the Fourier expansion of the relative permittivity in the hologram is expressed as:

$$\epsilon_r(x,y) = \sum_h \epsilon_h e^{jh\mathbf{Kr}} \tag{47}$$

where ϵ_h is the h-th Fourier component of the relative permittivity in the grating region and $\mathbf{K}$ is the grating vector, the magnitude of which is related to the grating period, Λ , as follows:

$$|\mathbf{K}| = \frac{2\pi}{\Lambda} \tag{48}$$

In the unslanted geometry expression, 47 can be converted into:

$$\epsilon_r(x) = \sum_h \epsilon_h e^{jhKx} \tag{49}$$

where it is assumed that the periodic relative permittivity varies in the x direction, parallel to the grating boundaries. The waves are assumed to propagate in the xy plane, with the electric field polarized in the z direction, so that TM polarization is studied.

It is further assumed here that the diffraction grating (medium II in Fig. 5) is embedded between two homogeneous media, I and III. If a plane wave impinges onto the hologram from medium I, the electric field in media I and III will be expressed as:

$$E^I = e^{\left[-j\left(k_{x_0}x+k_{y_0}y\right)\right]} + \sum_i R_i e^{\left[-j\left(k_{x_i}x-k^I_{y_i}y\right)\right]}, \tag{50}$$

$$E^{III} = \sum_i T_i e^{\left[-j\left(k_{x_i}x-k^{III}_{z_i}(y-d)\right)\right]}. \tag{51}$$

We define $k_{x_0} = k_0\epsilon_I^{1/2}\sin\theta$, $k_{z_0} = k_0\epsilon_I^{1/2}\cos\theta$, $k_0 = 2\pi/\lambda_0$, where θ is the angle of incidence in medium I, λ_0 is the free-space wavelength, ϵ_I is the relative permittivity of medium I, R_i is the amplitude of the i-th order backward-diffracted wave and T_i is the amplitude of the i-th order forward-diffracted wave. k_{x_i} is determined by the vector Floquet condition:

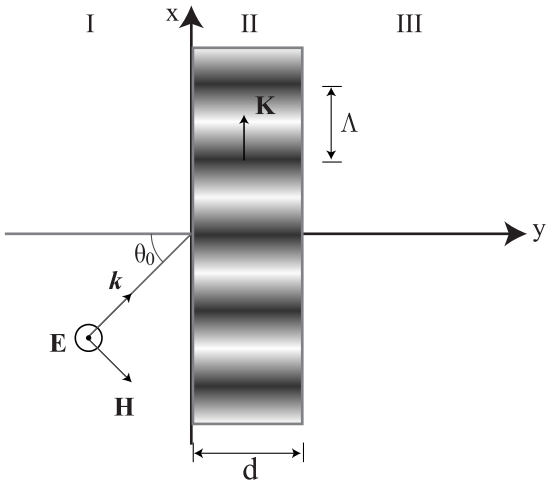

Figure 5: Scheme of a diffraction grating.

$$k_{x_i} = k_{x_0} - iK, \tag{52}$$

where the z components of the propagation vectors for the i-th orders are:

$$k^I_{z_i} = \left(k_0^2\epsilon_1 - k_{x_i}^2\right)^{1/2} \tag{53}$$

In the grating region the tangential electric (z component) and magnetic (x component) fields may be expressed as:

$$E_z^{II} = \sum_i S_{z_i}(y)e^{(-jk_{x_i}x)} \tag{54}$$

$$H_x^{II} = -j\left(\frac{\epsilon_0}{\mu_0}\right)^{1/2}\sum_i U_{x_i}(y)e^{(-jk_{x_i}x)} \tag{55}$$

Substituting equations (54) and (55) by equation (49) in Maxwell's equations, the following set of first order coupled equations can be derived:

$$\frac{\partial S_{z_i}}{\partial y} = k_0 U_{x_i} \tag{56}$$

$$\frac{\partial U_{x_i}}{\partial y} = \left(\frac{k_{x_i}^2}{k_0}\right)S_{yi} - k_0\sum_p \epsilon_{(i-p)}S_{yp} \tag{57}$$

The amplitudes S_{y_i} and U_{x_i} can be obtained by solving equations (56)-(57) using the formalism described in ref [21]. The $2\times N$ arbitrary constants that arise from the 2xN coupled equations (56),(57), where N is the number of orders retained, can be obtained by matching the tangential electric and magnetic field components at the two boundaries. Imposing the boundary conditions at the I-II and II-III interfaces permits the amplitudes of the backward waves, R_i, and of the forward waves, T_i to be calculated. The diffraction efficiencies for the different orders are expressed as:

$$\eta_u^R = R_i R_i^* Re\left(\frac{k_{z_{i1}}}{k_{z_0}}\right) \quad (58)$$

$$\eta_i^T = T_i T_i^* Re\left(\frac{k_{z_{i3}}}{k_{z_0}}\right) \quad (59)$$

4. Experiment

In this section, the results obtained via the FDTD method are compared with some well-known theoretical values. Firstly, several arrays of apertures are simulated. The results of the electric far-field are compared with the analytical irradiance in the Fraunhofer region. These simulations give us the opportunity to validate our numerical method in order to simulate more complicated optical structures such as volume holographic gratings. Secondly, numerical results of the volume holographic gratings are presented with their theoretical values, which are calculated using of the RCWT applied to periodic media.

4.1. Fraunhofer diffraction

The diffraction pattern produced by an array of apertures in the Fraunhofer region is a well known problem in optics. Due to the fact that closed analytical expressions exist in the Fraunhofer region for this type of configurations, the FDTD method can be validated comparing and contrasting curves obtained via FDTD simulation with analytical curves. In optical laboratory situations diffraction is mainly studied in the forward direction, that is, for small angles from the direction of propagation of the incident field. Furthermore, the distances are much larger than the wavelength λ, $r >> \lambda$. As a consequence, the irradiance pattern in the far-field region involves large distances and, as a result, bigger grids in the FDTD method must be simulated. However, the near-field to far-field transformation can be used to solve this problem.

A diagram of the systems chosen to be simulated is shown in Fig 6, where a defined number of apertures are displayed.

In Fig. 6, it can be seen how the apertures are modelled in the method by opening several slits in a perfect conductor plane. These slits are illuminated by a plane wave using the TF/SF formulation. The sampling plane contains the near-field values of the electromagnetic field to be propagated to the i-th point in the far-field (P^i_{far}).

For an array of N apertures, the analytical irradiance expression is:

$$\frac{I(0)}{N^2}\left(\frac{sin\beta}{\beta}\right)^2\left(\frac{sinN\alpha}{sin\alpha}\right)^2, \quad (60)$$

with $\beta = kb/2sin\theta$ and $\alpha = kd/2sin\theta$. The angle θ is established as the angle formed by the vector $\mathbf{r}_i^j$ (distance between the near-field point i and the far-field point j) and the normal of the output plane of the apertures.

The variable parameters such as the wavelength and the spatial period are fixed as λ=633 nm and $\Delta x = \lambda/10$. The diffraction pattern points must be situated at a distance from the slits satisfying Fraunhofer's far field condition $F = a^2/L\lambda \ll 1$.

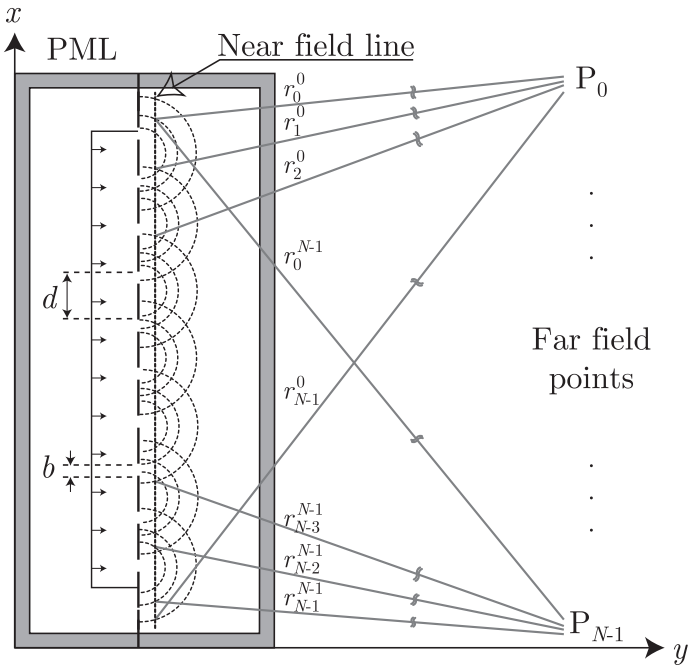

Figure 6: Diagram of an array of apertures simulation.

Where a is the width of the slit and L is the distance between the far field observation point (screen) and the plane slits. Distance L was established for all the simulations as 4000λ, satisfying the Fraunhofer's far field condition. The distant observation points were obtained by means of the near-field to far-field transformation (Section 2.3) along the x-coordinate at $y = 40000\Delta$. The irradiance patterns, which are proportional to the electric field, are computed by means of NF/FF propagation. A sampling plane near the output plane of the apertures array contains the near field that is propagated to the far field. The electric far-field values are calculated across a line placed at y = 4000 Δ. When a simulation finishes, the values of the electric far-field plane are available as a function of time. The modulus of the electric far field ($|E_z|$) as a function of time is shown in Fig. 7.b). From these values, the normalized irradiance can be easily derived as can be seen in 7.a).

In Fig. 8 the simulation results are compared with the analytical values. As can be seen from the graph, the results obtained via the FDTD method are a good enough fit to the analytical curves in the Fraunhofer region. This simulation validated our implementation of the FDTD method for optical wavelengths.

The numerical results were obtained by simulating of volume diffraction gratings in a two-dimensional grid. A grating with constant parameters, $n_0 = 1.63$, $\Lambda = 0.83$ μm was chosen. The thickness of the grating varied from 1 μm to 25 μm, and two refractive index modulation were chosen, $\Delta n = 0.025$ and $\Delta n = 0.015$. The wavelength of the incident wave was fixed at $\lambda = 633$ nm.

In order to minimize the diffractions at the borders of the total-field and the scattered field, the shape of the dielectric constants (related to the refractive index by $n = \sqrt{\epsilon_r}$) was modified

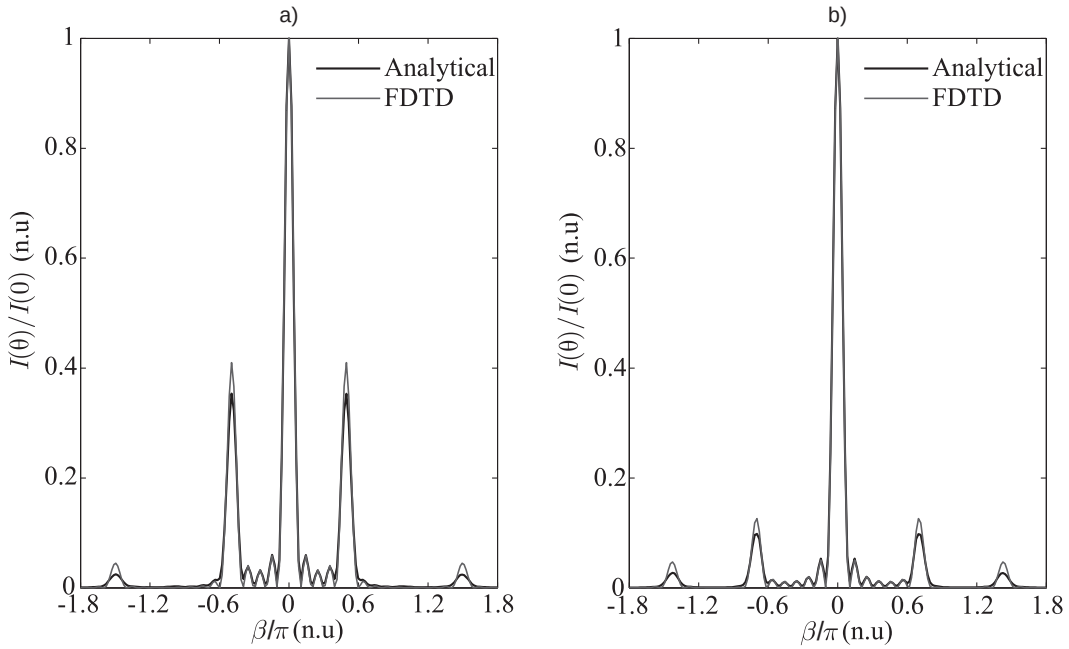

Figure 8: Normalized irradiance for N apertures with aperture width of a=50Δ and gap between apertures d=70Δ. a)N=5. b)N=7.

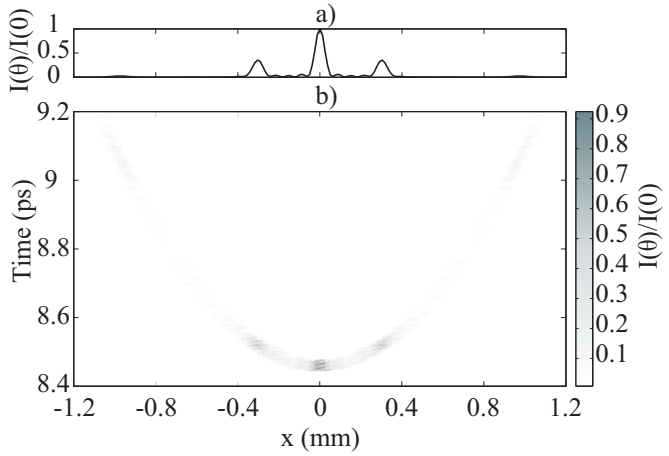

Figure 7: Electric far-field distribution (y=4000Δ) of an array of 5 apertures. a) Normalized irradiance . b) $|E_z|$ as a function of x and time

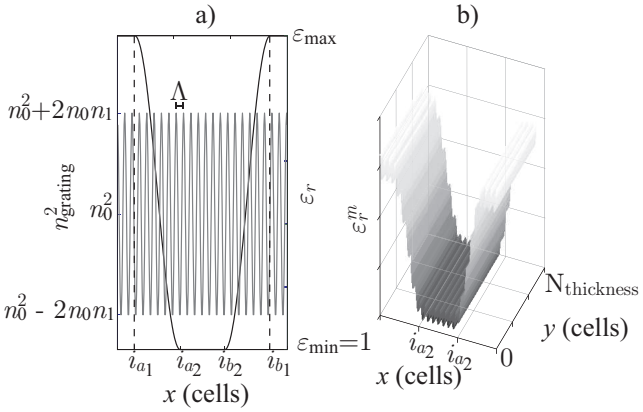

Figure 9: Electrical permittivity and conductivity after apply the tunneling masks. a) Electrical permittivity. b) Electrical conductivity.

at the borders of the simulation.

$$\epsilon_r = \begin{cases} \epsilon_{\max} & x < i_{a_1} \\ \epsilon_{\max}\cos\left(\frac{\pi}{2\cdot(i_{a_2}-i_{a_1})}(x-i_{a_1})\right)\cdot\epsilon_{\text{grating}} & i_{a_1} \geq x \leq i_{a_2} \\ \epsilon_{\text{grating}} \simeq n_0^2 + 2n_0n_1\cos\left(\frac{2\pi}{\Lambda}x\right) & i_{a_2} \geq x \leq i_{b_2} \\ \epsilon_{\max}\sin\left(\frac{\pi}{2\cdot(i_{b_1}-i_{b_2})}(x-i_{b_2})\right)\cdot\epsilon_{\text{grating}} & i_{b_2} \geq x \leq i_{b_1} \\ \epsilon_{\max} & x > i_{b_1} \end{cases} \quad (61)$$

The TF/SF formulation was designed to simulate structures that are completely confined inside the total region. Classical theory for diffraction gratings analysis considers in most cases an infinite grating. For our implementation of the FDTD

method, this approach cannot be assumed yet. Therefore the TF/SF must be formulated in zones where a dielectric medium is defined. Eq. (61) defines a dielectric structure that guides the light at the borders of the simulation region straight to the PML region in order to avoid undesired diffraction effects at the finite limits of our grating.

Fig. 9.a) shows the mask applied to the electrical permittivity and Fig. 9.b) its final tendency.

Furthermore, the TF-SF formulation was truncated in order to permit propagation of the plane waves along the diffraction grating without inherent numerical errors. TF/SF is truncated to avoid applying Eqs. (37) and (39) and to define j_b as the beginning of the diffraction grating. Since the "connecting condition" was removed in the plane $j = j_b$ the plane wave generated travels from the plane j_a to the end of the simulation region. The numerical errors produced at the interface between total field and scattered field are produced by linear interpolations necessary to obtain the values of the incident field. Interpolation is applied when the angle of incidence of the plane wave is different from 0 or 90.

All these modifications are shown in Fig. 10. More precisely Fig.10.a) show a diagram of the simulation before applying the permittivity masks and Fig.10.b) the result of a preliminary simulation with the undesired interference pattern. On the other hand, Fig. 10.c) to 10.f) shown several time steps of a simulation of the same phase grating with the improvement explained previously. It can be seen that the interference is tunneled to the PML region minimizing its contribution in the fields outside the grating. Transmitted and diffracted plane waves can be easily identified traveling in Bragg angles from the normal to the surface of the grating.

Regarding diffraction and angular efficiency results, all these parameters are obtained from the electric far-field pattern calculated in time-marching simulation from the values on the output surface of the grating. The electric far-field distribution is free of interference between transmitted ($m = 0$) and diffracted orders ($m = 1$). In Fig. 10.f) it can be seen how the plane waves corresponding with the transmitted and diffracted orders produce an interference pattern near to the output of the grating due to the interference of two plane waves.

The far-field distribution of the electric field is obtained by means of NF/FF propagation explained in section 2.3 avoiding enlarging the area of simulation. The plane where far field values are propagated was established at 80λ from the output plane of the grating.

Diffraction and transmission efficiency curves are represented in Fig. 11 and Fig. 12 for diffraction gratings of n_1=0.025 and n_1=0.015 respectively. The values obtained by the FDTD method are contrasted with the results of the RCW theory detailed in section 3. In all cases good agreement between the two methods is obtained.

The angular efficiency is calculated by means of several simulations in which the incidence angle is modified with respect to the Bragg condition defined as $\sin\theta'_0 = \lambda/2n_0\Delta$, where θ'_0 is related to the reconstruction angle inside the grating by Snell's law. In Fig.13 the values computed by the FDTD method for angular efficiency are shown for a grating with $n_1 = 0.025$. Also, values obtained by the method explained in section 3 are showed. Similar results are represented in Fig. 13 in which the refractive index modulation was established as $n_1 = 0.015$.

5. Conclusions

In this paper the FDTD method has been applied with successful results to analyze holographic gratings. More precisely, several volume diffraction gratings were simulated. In a first step, an experiment based on apertures permitted validation of the method in the Fraunhofer region. More precisely several arrays of apertures were simulated. In these cases, the far-field distribution permitted the irradiance pattern to be obtained, and this was compared with analytical curves. Once the method was validated, volume holographic gratings were simulated in order to study their diffraction and angular efficiency. In a similar manner, NF/FF propagation was applied to obtain the far-field distribution to avoid interference between orders at the output of the grating. The far-field distribution computed enabled the diffraction efficiency to be obtained, and this was compared with theoretical curves obtained using the RCWT. Moreover, the angular efficiency was analyzed and again good agreement was obtained between numerical and analytical curves.

Formalisms such as the perfectly matched layers and near-field to far-field propagation allowed the FDTD method to be applied to these optical devices with satisfactory results and low computational requirements.

On the other hand, several authors have encountered different drawbacks to applying the FDTD method to this type of devices, which are quite different from typical electromagnetic scattering structures. Making slight modifications to the TF/SF formulation and applying a mask to the electrical permittivity permitted the interference pattern produced in the interface region between total field and scattered field to be reduced as soon as the light in this area is guided to the PML layers.

Acknowledgements

This work was supported by the "Ministerio Ciencia e Innovacin" of Spain under project FIS2008-05856-C02-02, by the "Generalitat Valenciana" of Spain under project ACOMP/2010/156 and by the University of Alicante under the project GRE09-10.

Bibliography

[1] A. K. Richter, F. P. Carlson, Holographically generated lens, Applied Optics 13 (1974) 2924–2930.
[2] J. R. Magariños, D. J. Coleman, Holographic mirrors, Optical Engineering 24 (1985) 769.
[3] O. D. D. Soares, Holographic coupler for fiber optics, Optical Engineering 20 (1981) 740.
[4] T. Yagai, S. Kawai, H. Huang, Optical computing and interconnects, Proceedings of the IEEE 84 (1996) 828.
[5] H. J. Coufal, D. Psaltis, G. T. Sincerbox, Holographic Data Storage, Springer Verlag, Berlin, 2000.
[6] B. Lichtenberg, N. C. Gallagher, Numerical modeling of diffractive devices using the finite element method, Optical Engineering 33 (1994) 3518–3526.

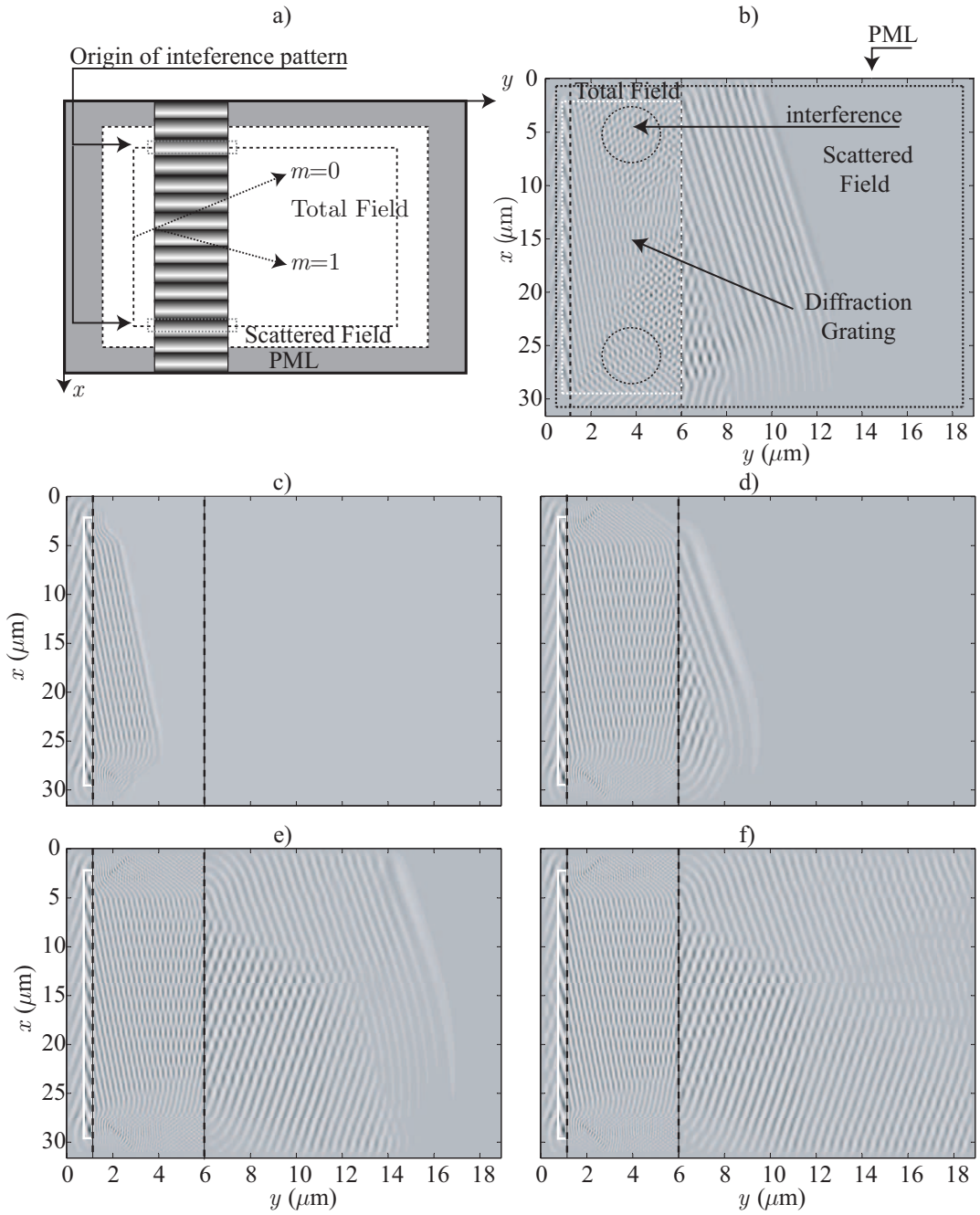

Figure 10: Electrical field (E_z) in a simulation of a phase grating with d=12.6 μm,n_0 = 1.63 and n_1=0.025. a) Scheme of the simulation without modifying the electrical permittivity shape at borders. b) Simulation showing the interference pattern produced at the border between diffraction grating and connecting conditions. c) Simulation without interference at 350 Δt.d) Simulation without interference at 700 Δt.e) Simulation without interference at 1000 Δt. f) Simulation without interference at 1500 Δt.

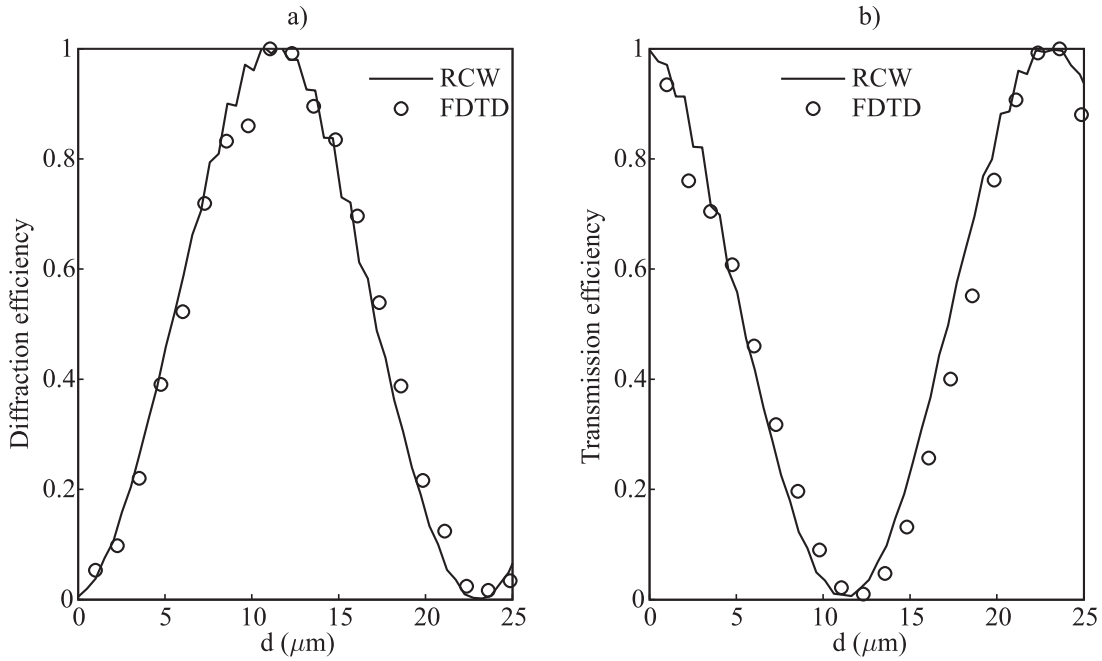

Figure 11: Comparison of numerical and analytical efficiency of a holographic grating with n_1=0.025. a) Diffraction efficiency (m = 1). b) Transmission efficiency (m = 0).

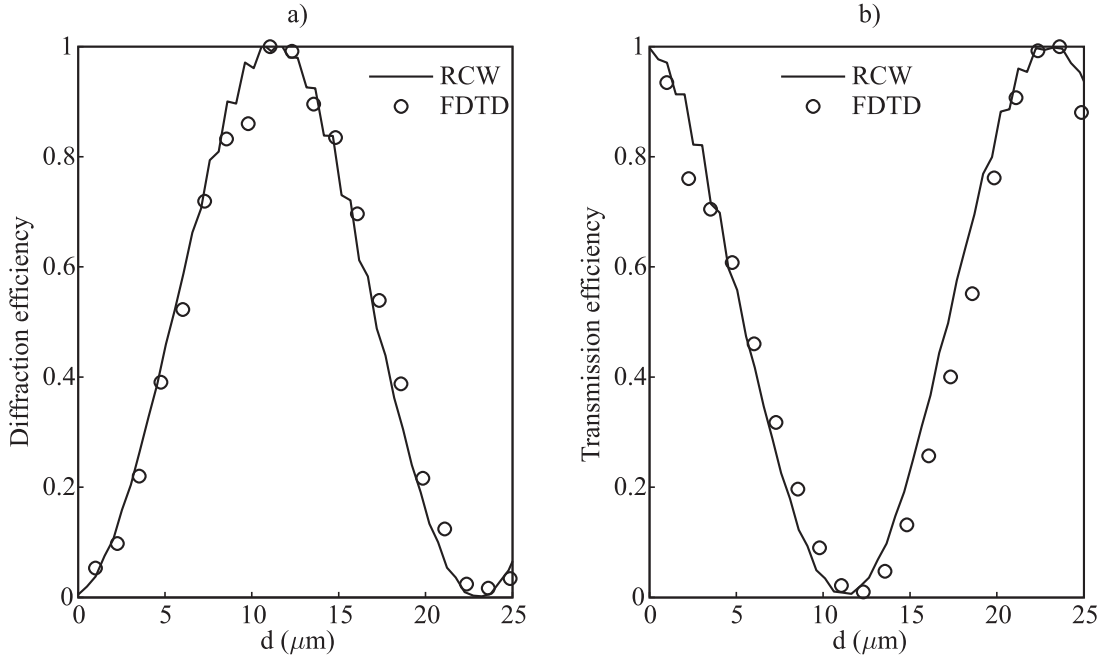

Figure 12: Comparison of numerical and analytical efficiency of a holographic grating with n_1=0.015. a) Diffraction efficiency (m = 1). b) Transmission efficiency (m = 0).

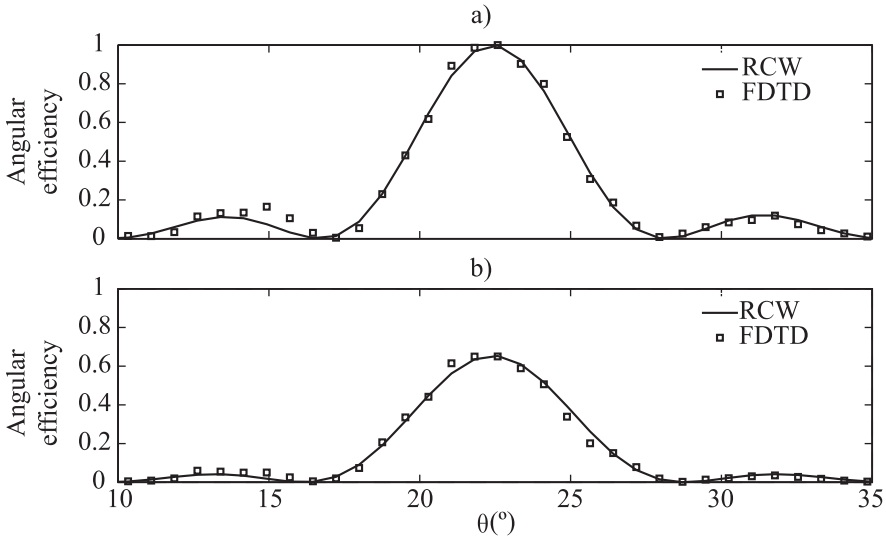

Figure 13: Angular selectivity of a phase grating showing the normalizad diffraction and transmission efficiency as a function of the incidence angle. a) Results for n_1=0.025. b) Results for n_1=0.015.

[7] K. Hirayama, E. N. Glytsis, T. K. Gaylord, Rigorous electromagnetic analysis of diffractive cylindrical lenses, J. Opt. Soc. Am. A 13 (1996) 2219–2231.

[8] J. M. Bendickson, E. N. Glytsis, T. K. Gaylord, Scalar integral diffraction methods: unification, accuracy, and comparison with a rigorous boundary element method with application to diffractive cylindrical lenses, Journal Optical Society of America A 15 (1998) 1822–1837.

[9] D. W. Prather, M. S. Mirotznik, J. N. Mait, Boundary element method for vector modeling-diffractive optical elements, in: I. Cindrich, S. H. Lee (Eds.), Diffractive and Holographic Optics Technology II, Vol. 2404, Proc. SPIE, 1995, pp. 28–39.

[10] D. W. Prather, M. S. Mirotznik, J. N. Mait, Boundary integral methods applied to the analysis of diffractive optical elements, J. Opt. Soc. Am. A 14 (1) (1997) 34–43.

[11] E. E. Kriezis, S. J. Elston, Finite-difference time domain method for light wave propagation within liquid crystal devices, Optics Communications 165 (1-3) (1999) 99–105.

[12] D. W. Prather, S. Shi, Formulation and application of the finite-difference time-domain method for the analysis of axially symmetric diffractive optical elements, J. Opt. Soc. Am. A 16 (5) (1999) 1131–1142.

[13] D. M. Sullivan, Electromagnetic Simulation using the FDTD Method, IEEE Press Editorial Board, 2000.

[14] A.Taflove, COMPUTATIONAL ELECTRODYNAMICS: The Finite-Difference Time-Domain Method, Artech House Publishers, 1995.

[15] S. González García, B. García Olmedo, R. Gómez Martín, A time-domain near- to far-field transformation for fdtd in two dimensions, Microwave and Optical Technology Letters 27 (6) (2000) 427–432.

[16] J. W. Goodman, Introduction to Fourier Optics, McGraw-Hill, New York, 1996, pp. 36-38.

[17] T. K. Gaylord, M. G. Moharam, Analysis and applications of optical diffraction by gratings, Proceedings of the IEEE 73 (5) (1985) 894–937.

[18] R. Petit, Electromagnetic Theory of Gratings, Springer-Verlag, Berlin, 1980.

[19] J. Turunen, F. Wrowski, Diffractive optics: from promise to fruition, in *Trends in Optics*, Academic, San Diego, Calif., 1996, Ch. 6, pp. 111–123.

[20] J. B. Judkins, R. W. Ziolkowski, Finite-difference time-domain modeling of nonperfectly conducting metallic thin-film gratings, J. Opt. Soc. Am. A 12 (9) (1995) 1974–1983.

[21] M. G. Moharam, E. B. Grann, D. A. Pommet, T. K. Gaylord, Formulation for stable and efficient implementation of the rigorous coupled-wave analysis of binary gratings, J. Opt. Soc. Am. A 12 (1995) 1068–1076.

[22] H. Kogelnik, Coupled wave theory for thick hologram gratings, The Bell System Technical Journal, Vol.˜48, no.˜9, November 1969, pp.˜2909-2947 48 (1969) 2909–2947.

[23] C. Balanis, Advanced Engineering Electromagnetics, New York: Wiley, 1989.

[24] K. Yee, Numerical solution of initial boundary value problems involving maxwell's equations in isotropic media, IEEE Trans. on Antennas and Propagation AP (17) (1966) 585–589.

[25] H. Ichikawa, Electromagnetic analysis of diffraction gratings by the finite-difference time-domain method, J. Opt. Soc. Am. A 15 (1) (1998) 152–157.

[26] K. S. Kunz, R. J. Luebbers, The Finite Difference Time Domain Method for Electromagnetics, CRC Press, 1993.

[27] J. Berenger, A perfectly matched layer for the absorption of electromagnetic waves, J. Comput. Phys 114 (1994) 185–200.

[28] F. Pérez-Ocón, J. R. J. Cuesta, A. M. P. Molina, Exponential discretization of the perfectly matched layer (pml) absorbing boundary condition simulation in fd-td 3d, Optik - International Journal for Light and Electron Optics 113 (8) (2002) 354 – 360.

[29] D. Sullivan, A simplified pml for use with the fdtd method, Microwave and Guided Wave Letters, IEEE 6 (2) (1996) 97–99.

[30] Z. Sacks, D. Kingsland, R. Lee, J.-F. Lee, A perfectly matched anisotropic absorber for use as an absorbing boundary condition, Antennas and Propagation, IEEE Transactions on 43 (12) (1995) 1460–1463.

[31] G. Mur, Absorbing boundary conditions for the finite-difference approximation of the time-domain electromagnetic field equations, IEEE Trans. Electromagnetic Compatibility 23 (1981) 377–382.

[32] Y. N. Yiang, D. B. Ge, S. J. Ding, Analysis of tfsf boundary for 2d-fdtd with plane p-wave propagation in layered dispersive and lossy media, Progress in Electromagnetic Research 83 (2008) 157–175.

[33] M. J. Barth, M. M. McLeod, R. W. Ziolkowski, A near and far-field projection algorithm for finite-difference time-domain codes, J. Electromag Waves Appl. 6 (1992) 5–18.

[34] K. L. Shlager, G. S. Smith, Near-field to near-field transformation for use with fdtd method and its application to pulsed antenna problems, Electron Lett 30 (1994) 1262–1264.

[35] K. L. Shlager, G. S. Smith, Comparison of two fdtd near-field to far-field transformations applied to pulsed antenna problems, Electron Lett 31 (1995) 936–938.

[36] R. J. Luebbers, K. S. Kunz, M. Schneider, F. Hunsberger, A finite-difference time-domain near zone to far zone transformation, IEEE Trans. Antennas and Propagation 39 (1991) 429–433.

[37] K. Yee, D. Ingham, K. Shlager, Time-domain extrapolation to the far field based on fdtd calculations, Antennas and Propagation, IEEE Transactions on 39 (3) (1991) 410–413.

[38] R. Luebbers, D. Ryan, J. Beggs, A two-dimensional time-domain near-zone to far-zone transformation, Antennas and Propagation, IEEE Trans-

actions on 40 (7) (1992) 848–851.
[39] W. Panofsky, M. Phillips, Classical electricity and magnetism, 2nd Edition, Addison-Wesley series in physics, CA, 1968.
[40] C. L. Bennett, Jr., A technique for computing approximate electromagnetic impulse response of conducting bodies, Ph.D. thesis, West Lafayette, IN, USA (1968).
[41] F. Xu, W. Hong, X. Zhu, A new time domain near field to far field transformation for fdtd in two dimensions, in: Microwave Symposium Digest, 2002 IEEE MTT-S International, Vol. 3, 2002, pp. 2057–2060.
[42] D. Maystre, A new general integral theory for dielectric coated gratings, J. Opt. Soc. Am. 68 (4) (1978) 490–495.
[43] F. Montiel, M. Nevière, Differential theory of gratings: extension to deep gratings of arbitrary profile and permittivity through the r-matrix propagation algorithm, J. Opt. Soc. Am. A 11 (12) (1994) 3241–3250.
[44] N. Uchida, Calculation of diffraction efficiency in hologram gratings attenuated along the direction perpendicular to the grating vector, J. Opt. Soc. Am. 63 (3) (1973) 280–287.
[45] J. T. Sheridan, L. Solymar, Diffraction by volume gratings: approximate solution in terms of boundary diffraction coefficients, J. Opt. Soc. Am. A 9 (9) (1992) 1586–1591.
[46] R. R. A. Syms, L. Solymar, Planar volume phase holograms formed in bleached photographic emulsions, Appl. Opt. 22 (10) (1983) 1479–1496.
[47] J. T. Sheridan, Generalization of the boundary diffraction method for volume gratings, J. Opt. Soc. Am. A 11 (2) (1994) 649–656.
[48] H. KOGELNIK, Bragg diffraction in hologram gratings with multiple internal reflections, J. Opt. Soc. Am. 57 (3) (1967) 431–433.